ACS APPLIED NANO MATERIALS

www.acsanm.org Article

Cuprous Oxide Cubic Particles with Strong and Tunable Mie Resonances for Use as Nanoantennas

Farshid Mohammadparast, Sundaram Bhardwaj Ramakrishnan, Nishan Khatri, Ravi Teja A. Tirumala, Susheng Tan, A. Kaan Kalkan, and Marimuthu Andiappan*

Cite This: *ACS Appl. Nano Mater.* 2020, 3, 6806–6815 Read Online

ACCESS | Metrics & More | Article Recommendations | SI Supporting Information

Downloaded via OKLAHOMA STATE UNIV STILLWATER on October 13, 2020 at 15:35:23 (UTC).
See https://pubs.acs.org/sharingguidelines for options on how to legitimately share published articles.

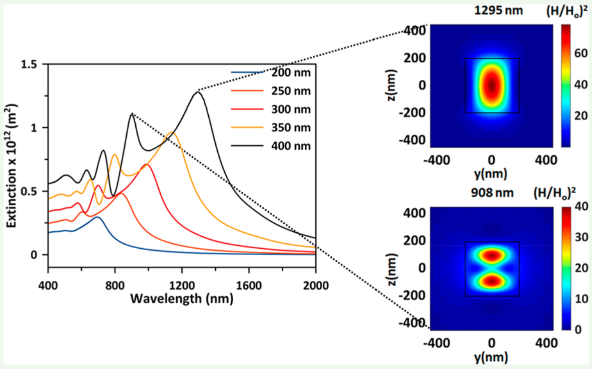

ABSTRACT: The ability of plasmonic metal nanostructures (PMNs), such as silver and gold nanoparticles, to manipulate and concentrate electromagnetic fields at the nanoscale is the foundation for wide range of applications, including nanoscale optics, solar energy harvesting, and photocatalysis. However, there are inherent problems associated with plasmonic metals, such as high Ohmic losses and poorer compatibility with the conventional complementary metal−oxide−semiconductor (CMOS) microfabrication processes. These limitations inhibit the broader use of PMNs in practical applications. Herein, we report submicrometer cuprous oxide (Cu_2O) cubic particles can exhibit strong electric and magnetic Mie resonances with extinction/scattering cross sections comparable to or slightly exceeding those of Ag particles. Using size- and shape-controlling particle synthesis techniques, optical spectroscopy, and finite-difference time-domain simulations, we show that the Mie resonance wavelengths are size- and shape-dependent and tunable in the visible to near-infrared regions. Therefore, submicrometer Cu_2O cubic particles may potentially emerge as high-performance alternatives to PMNs. The strong electric and magnetic Mie-resonance-mediated nanoantenna attribute of the Cu_2O cubic particles can be potentially used in a wide range of applications, including nanoscale optics, surface-enhanced Raman spectroscopy, surface-enhanced infrared absorption spectroscopy, photocatalysis, and photovoltaics.

KEYWORDS: *cuprous oxide, cubes, dielectric resonance, magnetic field, electric field*

■ INTRODUCTION

Plasmonic metal nanostructures (PMNs), such as silver (Ag) and gold (Au) nanoparticles, exhibit extraordinarily high extinction cross sections due to localized surface plasmon resonances (LSPRs).[1−12] Because the LSPR wavelength is sensitive to the geometry and physical environment, PMNs are very attractive for real-world applications such as sensors,[6,8] nano- and micro-optical devices,[13] photocatalysis,[14−20] and photovoltaics.[21−24] Also, the strong interplay between plasmonic nanostructures and metamaterials has led to realization of exceptional properties such as artificial magnetism,[25−27] finding applications in subwavelength resonant cavities, subdiffraction near-field superlenses, and phase compensators,[28] smart metamaterial cloaking,[29−31] and plasmonic color printing and optical data storage.[32]

By virtue of their high extinction cross sections with resonances in the visible and near-IR, PMNs can act as nanoantennas via the electromagnetic (EM) field enhancement effect which has promising applications in third-generation photovoltaics such as dye-sensitized, organic, and quantum dot- and perovskite-based solar cells.[21,22] However, these noble metals (Ag and Au) are scarce and expensive and pose limitations such as intrinsic nonradiative optical losses and fabrication complexities.[30] To overcome this barrier, recent years have witnessed a growing interest in developing novel nonplasmonic and low-loss dielectric resonators that can support light manipulation at the nanoscale and exhibit strong extinction cross sections.[33]

While plasmonic metal[1−11] and metal oxide[34,35] spheres exhibit only electric multipolar resonances (i.e., dipole, quadrupole, etc.), for optically resonant dielectric spheres, both electric and magnetic multipolar resonances occur.[33,36,37] Similar to the electric multipolar modes in plasmonic nanoparticles, the electric and magnetic multipolar modes in dielectric structures can lead to enhanced optical responses, such as surface-enhanced absorption, fluorescence, and Raman scattering.[33] Therefore, optically resonant submicrometer

Received: May 2, 2020
Accepted: June 9, 2020
Published: June 9, 2020

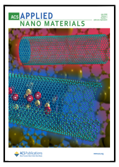

ACS Publications © 2020 American Chemical Society

https://dx.doi.org/10.1021/acsanm.0c01201
ACS Appl. Nano Mater. 2020, 3, 6806−6815

Scheme 1. A Pictorial Description of Synthesis of (a) Spherical Cu_2O Particles Using Microemulsion Method and (b) Cubic Cu_2O Particles Using wet Chemical Reduction Method

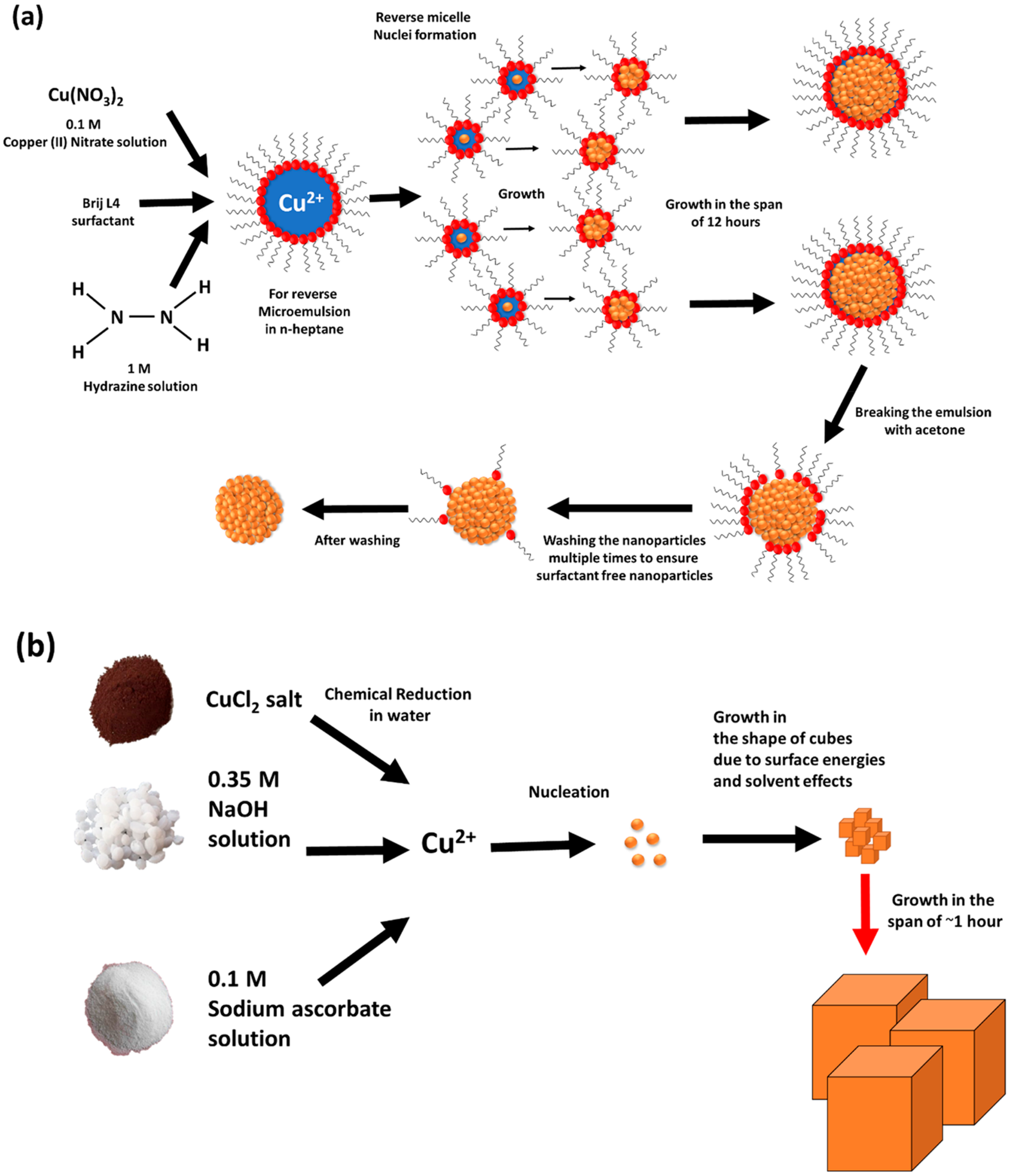

dielectric particles have recently emerged as high-performance alternatives to PMNs. For example, it has been demonstrated that submicrometer silicon (Si) sphere resonators exhibit lower dissipation losses, strong localization and enhancement of electromagnetic fields, and superior performance in comparison to their lossy plasmonic silver counterparts.[33,38,39] Also, strong electric and magnetic multipolar resonances have recently been demonstrated in various dielectric nanostructures, such as Si hollow nanocylinders and nanodisks,[40] nanowires,[41−43] silicon carbide microrods,[44] GaAs nanodisks,[45] tellurium cubes,[46] germanium particles,[47] and cuprous oxide (Cu_2O) spherical,[48] truncated octahedral,[49] and hollow spherical particles.[50]

Herein, we report strong and tunable nonplasmonic Mie resonances in Cu_2O cubes with sizes of a few hundred nanometers. Using finite-difference time-domain (FDTD) simulations, we show that the Cu_2O cubes exhibit strong localization and enhancement of electric as well as magnetic fields at the Mie resonances. We show experimentally and numerically that Mie resonances in Cu_2O cubes can be tuned from visible to near-infrared (NIR) by varying their size. Specifically, the high scattering cross sections of the Cu_2O cubes allow for acquisition of single particle scattering spectra, which are also observed to vary with particle size. The novel findings of this contribution are (i) strong and size-tunable Mie resonances in Cu_2O cubes and (ii) exceptionally high scattering cross sections of Cu_2O cubes as predicted and corroborated by FDTD simulations and single particle scattering spectroscopy, respectively. In particular, we have demonstrated the dielectric Cu_2O cubes can exhibit strong electric and magnetic Mie resonances with scattering cross sections comparable to or slightly exceeding those of plasmonic Ag nanoparticles. Finally, (iii) the scattering cross sections of Cu_2O cubes are higher than those of spheres (per same size) by using single-particle scattering spectroscopy and FDTD simulations.

■ RESULTS AND DISCUSSION

To experimentally demonstrate the strong and tunable Mie resonances of the Cu_2O cubic particles and compare their extinction and scattering cross sections with those of spheres, we synthesized spherical and cubic particles of Cu_2O. The synthesis procedure followed a microemulsion method for the Cu_2O spherical particles, as shown schematically in Scheme 1a. While for the cubes, as shown schematically in Scheme 1b, a wet chemical reduction route was employed. The detailed synthesis procedures are described in the Supporting Information.

The Cu_2O phase for both quasi-spherical and cubic particles is confirmed by the X-ray diffraction (XRD) patterns, as shown in Figure S1a,b.[20,51] The Cu_2O crystalline phase of single nanocubes are also confirmed by using single-particle Raman spectroscopy. Figure 1 shows a representative Raman fingerprint of a single nanocube, which conforms to the Cu_2O crystalline phase.[52−55] The cutoff of the Raman intensity below 200 cm^{-1} is due to the dichroic laser mirror of the microscope (the Rayleigh rejection filter cutoff is at 90 cm^{-1}). The diffraction-limited bright-field image of the nanocube is shown in the inset. The strongest peak, being at 217 cm^{-1}, is a second-order Raman peak, assigned to the overtone of the $\Gamma_{12}^{(-)}$ mode, and is characteristic of crystalline Cu_2O.[52,53] The second strongest peak, seen at 629 cm^{-1}, is assigned to the T_{1u} symmetry lattice vibration in Cu_2O which is infrared-active.[52] The 417 cm^{-1} peak, being the third strongest, is attributed to the overtone of four phonons, $3\Gamma_{12}^{-} + \Gamma_{25}^{-}$, in crystalline Cu_2O.[52] On the other hand, the strongest characteristic peaks of CuO, being at 298, 330, and 602 cm^{-1}, are not detected,[56] unless the incident laser power is increased beyond 0.46 mW, upon which transformation to the CuO phase occurs enabled by the excessive laser heating. The weaker peak at 522 cm^{-1} is assigned to the 3-fold degenerate T_{2g} mode.[54,55] Additionally, the peaks at 292 and 317 cm^{-1} appear to be a doublet associated with the 308 cm^{-1} Raman band in crystalline Cu_2O, which is assigned to the second overtone of the $\Gamma_{15}^{(-)}$ mode.

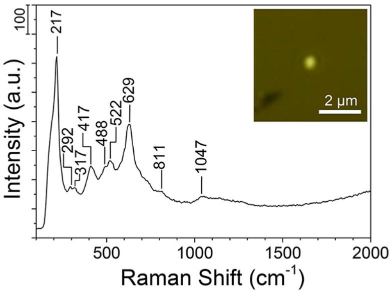

Figure 1. Raman scattering spectrum, acquired from a single Cu_2O nanocube. The inset shows the diffraction-limited bright-field image of the nanocube.

The Cu_2O cubic particles are also characterized by using high-resolution transmission electron microscopy (HR-TEM), selected area electron diffraction (SAED), and single-particle Raman spectroscopy. Figure 2a demonstrates a representative TEM image and SAED (inset). Additionally, Figure 2b depicts a HR-TEM image obtained from [110] zone axis and its related fast Fourier transform spectrum (FFT, inset). Both SAED and HR-TEM demonstrate that the synthesized Cu_2O nanoparticles are single-crystalline cubes.

Figures 2c and 2e show the UV−vis−NIR extinction spectra of Cu_2O sphere and cube samples measured at different times during the synthesis. We also measured the size distribution of the particles using TEM for samples obtained at different times during the synthesis (see Tables S2 and S3 as well as and Figures S2a−g). Figures 2d and 2f show the representative TEM images of the Cu_2O sphere and cube samples, respectively. During the Cu_2O spherical particle synthesis, we monitored the extinction spectrum as a function of synthesis time until 20 h, after which no significant change was observed. Additionally, the TEM indicated the average particle size increases with synthesis time and saturates beyond 20 h, being consistent with the extinction results. Similarly, for Cu_2O cubes, the change in the extinction spectra and the increase in average particle size were observed until 1 h and 15 min of synthesis, after which no further change was noticed. Therefore, the measured extinction spectra in Figures 2c and 2e verify the Mie resonances as well as their tunability with particle size and shape. As seen from Figure 2c, no resonance peaks for smaller Cu_2O spherical particles at the early stage of synthesis (e.g., 1 h sample, particle diameter = 5.3 ± 1.7 nm) can be captured in the measurement range of 300−800 nm. On the other hand, the 8 h sample with a size of 125 ± 28 nm shows a clear Mie resonance peak at about 450 nm. In the extinction spectra of Figure 2e, which monitors the time evolution of Cu_2O cubic particles, higher order multipole Mie resonances are also observed. For example, the 5 min sample, consisting of Cu_2O cubes of 267 ± 83 nm size, shows two distinct resonance peaks at 675 and 540 nm. With increasing synthesis time, the average particle size is increased, and the modes are red-shifted. For example, the end-of-synthesis cube sample (i.e., 1 h and 15 min sample, edge = 327 ± 125 nm) exhibits lower-energy-shifted Mie resonance peaks compared to that of the 5 min cube sample. Similarly, a lower energy shift of the peaks with increasing particle size is seen in Figure 2c and Figure S2d for the spherical particles.

To understand the nature of Mie resonances observed in the extinction spectra of Cu_2O spherical and cubic particles (Figures 2c,e), FDTD simulations are performed. The detailed FDTD simulation procedures are described in the Supporting Information. Figures 3a−d show the simulated extinction cross section spectra for varying sizes of Cu_2O spheres and cubes. The corresponding scattering and absorption spectra are shown in Figures S3a−d and S4a−d, respectively. In Figure 3a, a Mie resonance peak is seen to red-shift with increasing particle size. The peak maximum enters the simulation window of 400−2000 nm for particle size of 125 nm and larger. In Figure 3b, as the particle size increases to 200 nm and above, more than one of the Mie resonance peaks become noticeable. For the largest spherical particle of 400 nm diameter, three of the resonance peaks are below the bandgap of Cu_2O (i.e., wavelength above 590 nm). Cu_2O is a semiconductor with bandgaps of ~2.1 eV.[20] These resonance features are not expected for the bulk single crystalline Cu_2O. As seen from Figure 3c,d, there is a similar trend for Cu_2O cubic particles as well. For both spheres and cubes, with increasing particle size, the resonances downshift in energy. Upon comparison of spherical and cubic particles of similar sizes, the resonance peaks are lower energy shifted for cubic particles. From the simulated scattering and absorption spectra shown in Figures S3a−d and S4a−d, it is concluded that scattering is the dominant contribution to Mie extinction for the investigated particle sizes.

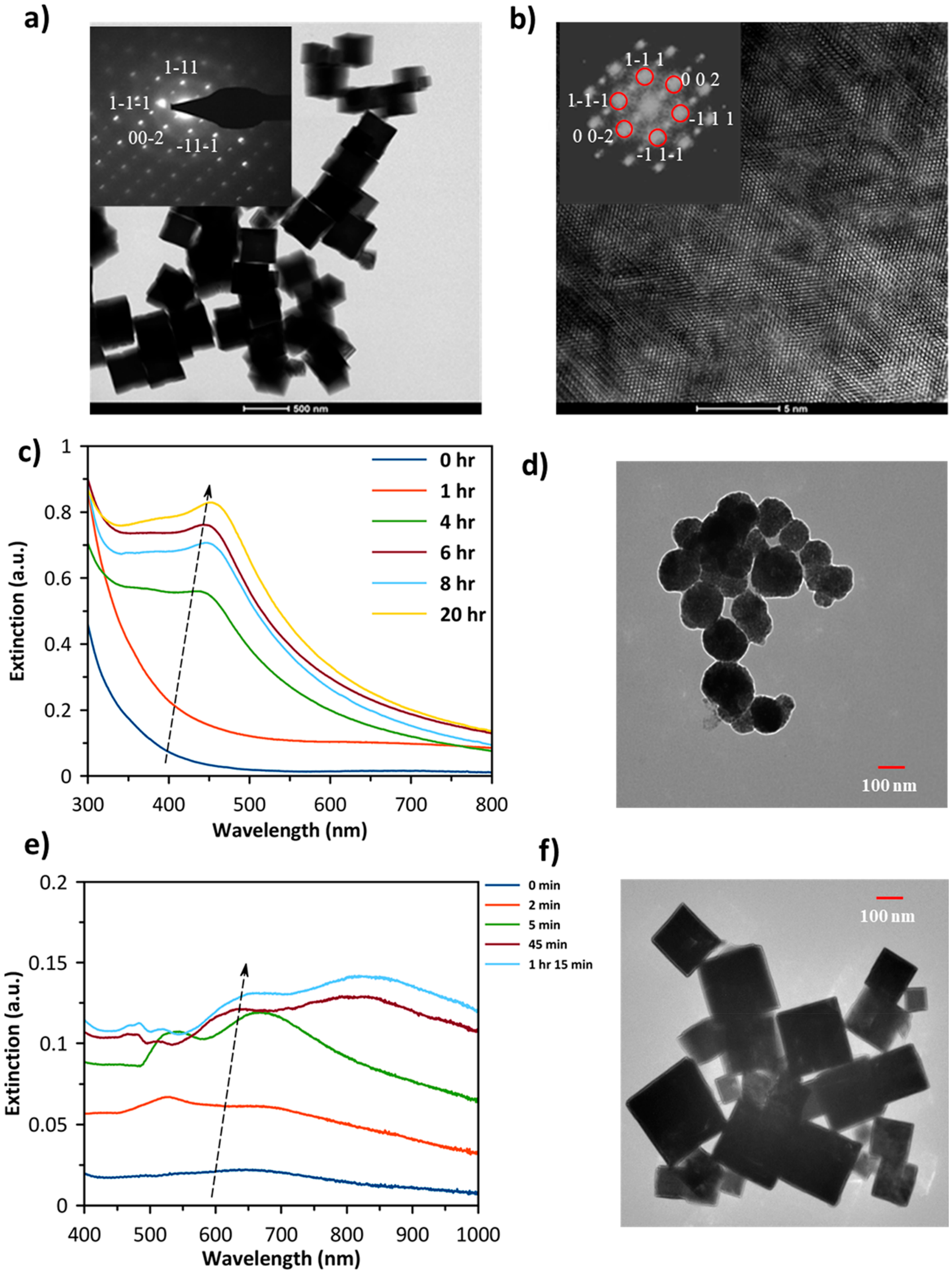

Figure 2. (a) Representative TEM image of cubic Cu_2O nanoparticles (inserted is a SAED from zone [110] of a single Cu_2O cube). (b) High-resolution TEM image of a cube with FFT spectrum inserted. (c, e) Measured UV−vis−NIR extinction spectra of Cu_2O spherical particles (c) and Cu_2O cubes (e) after different synthesis times. The arrows show the direction of time. (d, f) Representative TEM images of Cu_2O spheres after 8 h of synthesis (d) and Cu_2O cubes after 1 h and 15 min of synthesis (f). The legends in (c) and (e) show the synthesis times. Indexes shown in the inset of (b) match with the indexes shown in the inset of (a).

To explicate the Mie resonance peaks observed in the extinction spectra of Cu_2O spherical and cubic particles, we first present detailed analysis of the simulation data for the 175 nm spherical particle, as an example. Figure 4a shows the simulated extinction spectrum of the 175 nm diameter Cu_2O sphere. For comparison, we have also provided the simulated extinction spectrum of a 175 nm diameter Ag sphere in Figure 4b. The Cu_2O particle exhibits one resonance peak, being at 542 nm. In Figures 4c and 4d, we show the corresponding magnetic and electric field spatial distributions, respectively. For the simulations of the field distributions, a plane wave is used for the incident radiation propagating in the direction of positive *x*-axis and polarized along the *y*- and *z*-axes for the electric and magnetic fields, respectively.

The electric field distribution in Figure 4d shows the typical two-lobe distribution, characteristic of an electric dipole.

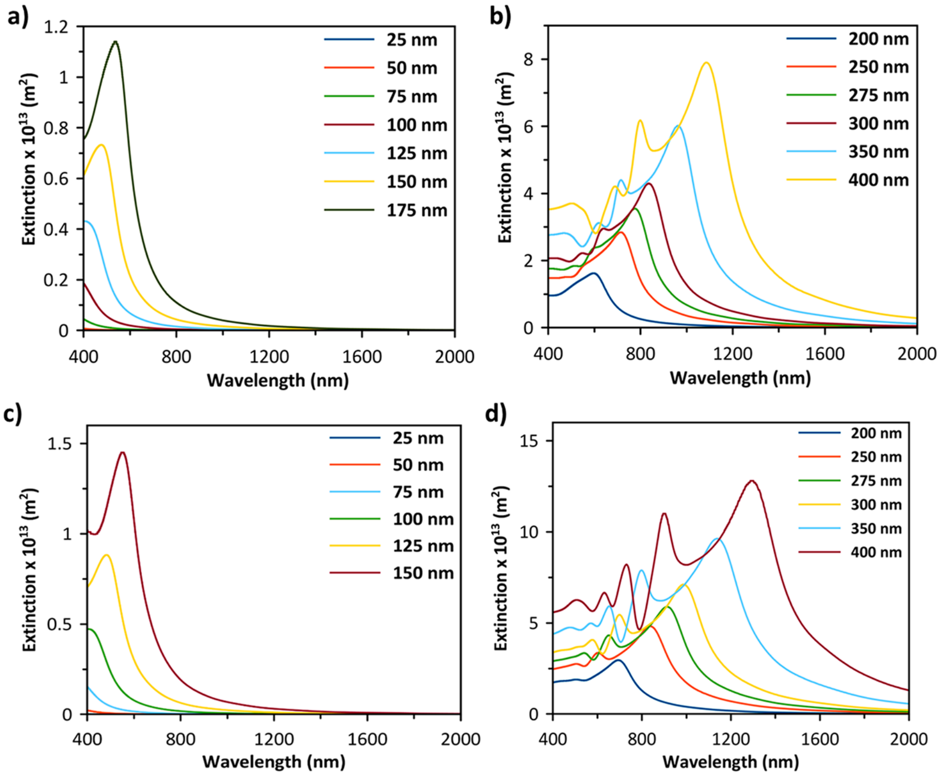

Figure 3. (a, b) Simulated extinction cross section as a function of wavelength for Cu_2O spheres of various diameters ranging from (a) 25 to 175 nm and (b) 200 to 400 nm. (c, d) Simulated extinction cross section as a function of wavelength for Cu_2O cubes of various edge lengths ranging from (c) 25 to 150 nm and (d) 200 to 400 nm. The propagation direction of the incident radiation for cubes simulation is perpendicular or parallel to the principal axes.

Similarly, the magnetic field distribution pattern in Figure 4c confirms the magnetic dipole mode.[38] The enhanced magnetic near field pictured in Figure 4c is generated by the circular displacement currents, strongly coupled to the electric field penetrating into the particle.[33] The optimum current-field overlap/coupling leading to magnetic dipole resonance occurs when the electric field is antiparallel at opposite edges of the particle. Hence, the condition for magnetic dipole resonance is that wavelength inside the particle equals approximately the particle dimension along the propagation direction (inside particle),[33] explaining the tunability of the resonance with size.

Figures 4c,d also show that the 175 nm Cu_2O sphere can exhibit enhancements of up to 25 and 8 times for the near magnetic and electric field intensities, respectively, over the incident far field. The comparison of the magnetic and electric field distributions shown in Figures 4c,d and Figures S5a,b confirms that the magnetic and electric dipole resonances both occur near 542 nm. For comparison, in Figures 4e,f, we also provide the simulated magnetic and electric field distributions for a 175 nm diameter Ag sphere at the LSPR peak wavelength of 530 nm (also see Figures S5c,d). As seen, the magnetic field enhancement is relatively weak for the Ag particle. Hence, the electric dipolar mode dominates the LSPR at 530 nm. Impressively, the extinction cross section of the Cu_2O sphere is comparable to that of the Ag sphere.

To distinguish the origin of multiple Mie resonance peaks observed in the extinction spectrum of larger Cu_2O particles, for example, 400 nm cubic particle in Figure 3d, we analyzed the magnetic and electric field distributions at multiple wavelengths around the lowest and second lowest energy resonance peaks. Figures 5a and 5b show the representative magnetic and electric field distributions, respectively, for the 400 nm Cu_2O cubic particle at the lowest energy Mie resonance (1295 nm). Figures 5a and 5b also show that the 400 nm Cu_2O cubic particle can exhibit localization and enhancement of up to 60 and 14 for the near magnetic and electric field intensities, respectively, over the incident far field. From the FDTD simulation results shown in Figures 5a,b along with the results shown in Figures S6a,b, S7, and S8, it can be concluded that the lowest energy Mie resonance peak is due to the combination of the magnetic and electric dipole excitations. To elucidate the second-lowest energy Mie resonance peak (908 nm) observed in the extinction spectrum, in Figures 5c,d, we display the magnetic and electric field distributions at 908 nm. From Figures 5c,d and Figures S6c,d, it is concluded that both the magnetic and electric quadrupole excitations contribute to this resonance peak.

In Figures 3a−d, upon comparison of spherical and cubic particles of similar sizes, the resonance peaks are lower energy shifted for cubic particles. We attribute these trends to the expected red-shifts of both the electric and magnetic resonance modes for cubic geometry.[3,57] Specifically, in cubic geometry, the surface charges responsible for the electric resonance modes are expected to accumulate at the corners. The increased charge separation reduces the restoring force for the surface charges, which results in a shift of the electric resonance modes toward lower energy.[3,57] For magnetic resonance modes, the resonant wavelength mainly depends on the radius of displacement current circle excited by the electric field. The radius of the displacement current circle is expected to be pushed outward with the increased effective radius of the cubic geometry due to the corners and leading to

https://dx.doi.org/10.1021/acsanm.0c01201
ACS Appl. Nano Mater. 2020, 3, 6806−6815

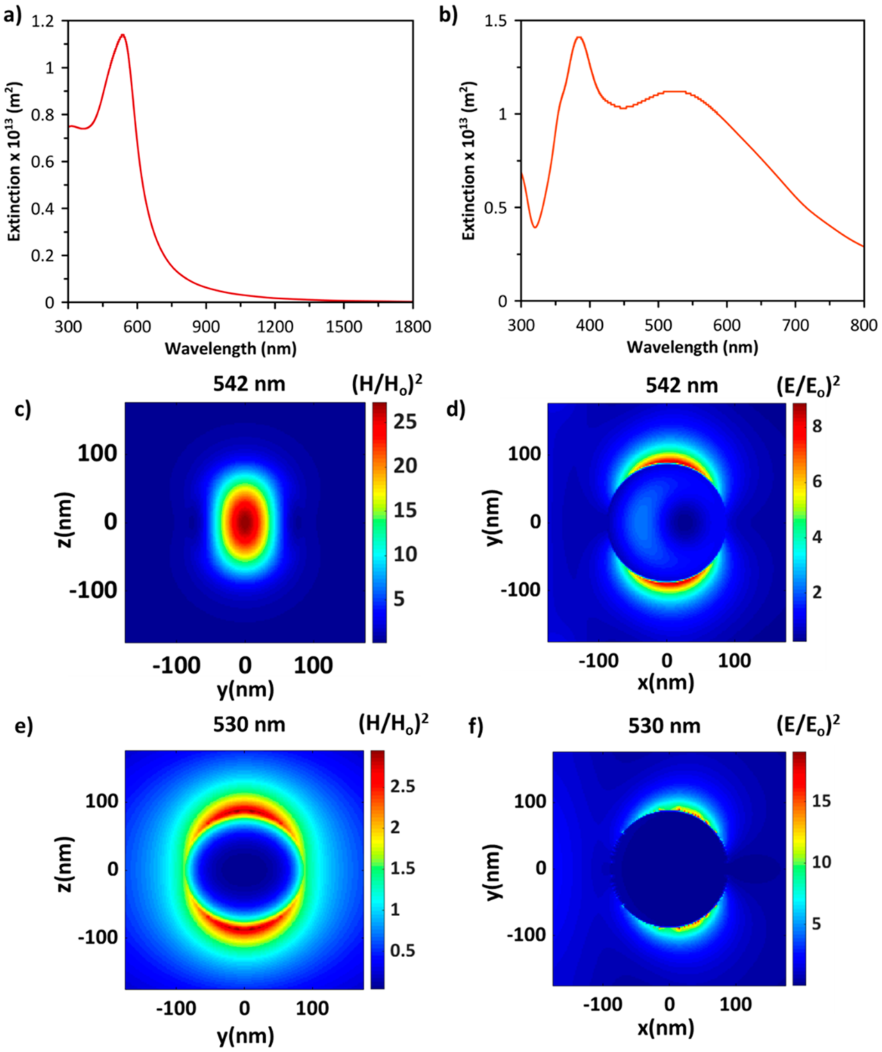

Figure 4. Simulated extinction cross section as a function of wavelength for the (a) 175 nm Cu_2O sphere and (b) 175 nm Ag sphere. Simulated spatial distribution of enhancement in (c) magnetic field intensity $[H^2/H_0^2]$ in the YZ plane and (d) electric field intensity $[E^2/E_0^2]$ in the XY plane for the 175 nm Cu_2O sphere at the resonance wavelength of 542 nm. Simulated spatial distribution of enhancement in (e) magnetic field intensity $[H^2/H_0^2]$ in the YZ plane and (f) electric field intensity $[E^2/E_0^2]$ in the XY plane for the 175 nm Ag sphere at the resonance wavelength of 530 nm.

the red-shift of magnetic resonance modes as well.[57] Because both the electric and magnetic resonance modes contribute to the Mie resonance peaks in Figures 3a–d, the peaks are lower energy shifted for cubic geometry.

The strong and tunable Mie resonances of Cu_2O cubic particles are also confirmed and compared with those of spherical particles by using single particle scattering spectroscopy. Specifically, to validate the high scattering cross sections, we have acquired Mie scattering spectra of single particles. The single particles were excited using a dark field condenser at glancing incidence (18°) to the substrate uniformly from all directions. The light scattered to far field in the semi-infinite space around the particle (above the substrate) was collected by a high numerical aperture lens. The details of the experimental setup, sample preparation, and acquisition are described in the Supporting Information. The acquisitions were performed for more than 30 spherical particles and cubes each. Figures 6a,b provide representative results.

Scattering spectra for three submicrometer spherical particles are given by Figure 6a. The corresponding SEM and diffraction-limited dark field images for each particle are also shown. The spectra reveal a systematic increase of the scattering cross section with size, but a concomitant red-shift is minor unlike in the simulated scattering spectra (Figures S3a,b). The steeper fall (i.e., cutoff) of the broad band above 2.6 eV (580 nm), marking its asymmetry, may be owed to enhanced absorption over the Cu_2O direct gap due to dipolar resonance in the particle. Such a quantum mechanical effect would be missed by the simulator, which borrows the dielectric function from bulk Cu_2O. Indeed, our scattering spectra are in agreement with ensemble-averaged extinction spectra of Figure 2c, which also exhibit asymmetry due to enhanced absorption below 580 nm as well as minor red-shift with increasing size. We assign the longer wavelength side of the broad feature in the scattering spectra to the preresonance tail of the magnetic and electric multipole resonances. In Figure 6a, the peaks of these resonances for particles II and III are possibly masked by the cutoff, discussed above.

Similarly, scattering spectra for three submicrometer cubes are shown in Figure 6b. By comparison with Figure 6a, a higher scattering cross section is inferred for Cu_2O cubes than spherical particles per equal size. Such high cross sections account for the remarkable signal-to-noise in Figure 6b. As an example, the peak scattering cross section, associated with the

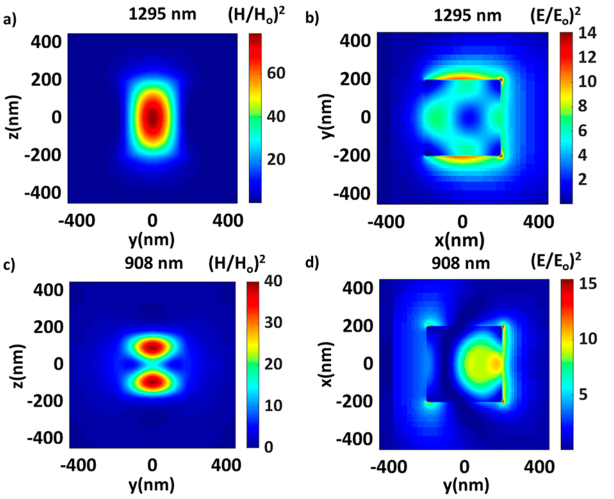

Figure 5. Simulated spatial distribution of enhancement in (a, c) magnetic field intensity [$H^2/H_0{}^2$] in the YZ plane and (b, d) electric field intensity [$E^2/E_0{}^2$] in the XY plane for Cu_2O cubes of 400 nm edge length at the resonance wavelength of (a, b) 1295 nm and (c, d) 908 nm.

lowest energy resonance band for particle III in Figure 6b (at 750 nm), is computed (Supporting Information) as 4.8 × 10^{-13} m^2, which is close to its simulated value of 6.3 × 10^{-13} m^2 (Figure S4b), while the maximum cross section for the same particle occurs at 634 nm, being 6.4 × 10^{-13} m^2. To benchmark these cross sections against those of plasmonic nanoparticles, we performed simulations for 300 and 400 nm Ag spheres as well as cubes (Figures S9−S12). As a result, our simulated extinction and scattering cross sections for Cu_2O spheres and cubes are comparable to or slightly exceeding those of Ag spheres and cubes, respectively. Here, we observe all the anticipated (i.e., by simulations) consequences of the increasing particle size: increasing cross section, lower energy shift of the resonances, and emergence/bolstering of the higher order multipole resonances. Despite the agreement in these trends, the measured spectra (Figure 6b) exhibit some differences from the simulated spectra (Figures S4a,b). First, the measured resonances are blue-shifted with respect to simulated ones. The second difference is that experimental spectra reveal higher number of resonance peaks than the simulated ones. For example, Figure S13 shows the comparison of FDTD simulation results performed with an incidence along the body diagonal of cubic particle and an incidence along the principal axis. As seen from Figure S13, the second lowest energy Mie resonance mode appears at different wavelengths for the two cases. For the cubic particle with an incidence along the principal axis, the second lowest energy Mie resonance mode is blue-shifted. Therefore, we attribute the higher number of resonances observed in Figure 6b to the excitation of the higher number of modes in the cube due to the larger range of incident directions. Specifically, in the measurement, the incidence is not only oblique to the substrate (XY plane), but it is in all directions rotationally symmetric around the Z-axis of the cube. Hence, the cube is excited at a range of incident angles. On the other hand, the additional peaks are not due to splitting of degenerate modes in the cube because of substrate-induced broken symmetries. We simulated cases with a glass substrate, but its influence on resonance wavelengths is found to be negligible. We will perform further simulations and single particle scattering measurements in future work to elucidate why experimental spectra are blue-shifted with respect to simulated spectra and to investigate the additional modes as well as their excitation dependence on incidence direction/polarization.

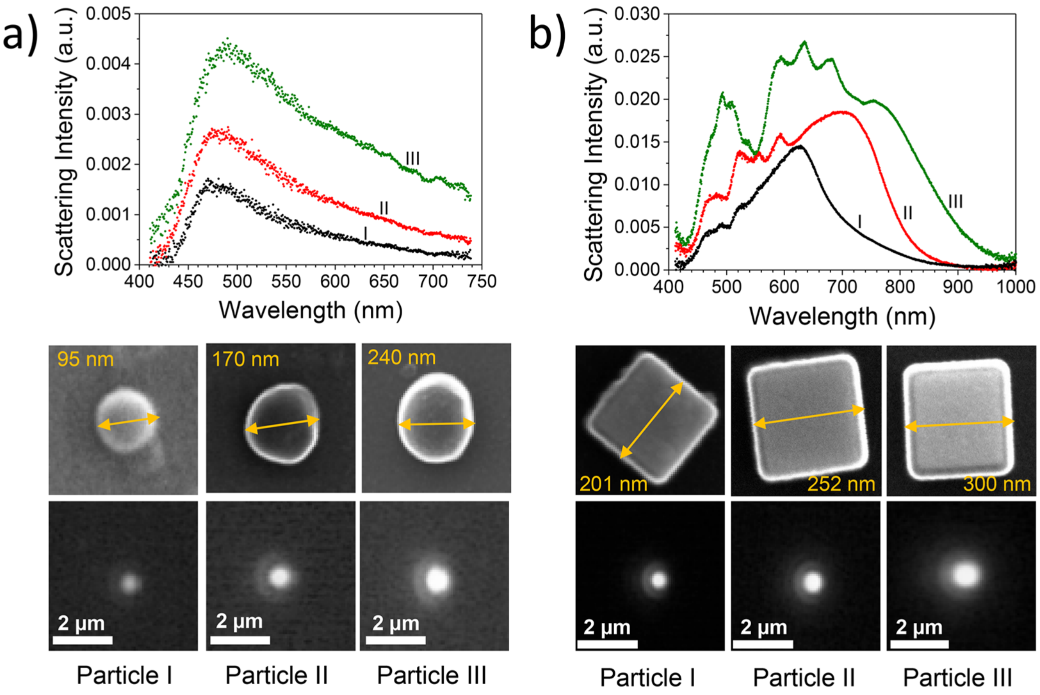

Figure 6. Scattering spectra of (a) three Cu_2O submicrometer spherical particles and (b) three Cu_2O submicrometer cubes. The corresponding SEM and diffraction-limited dark field images for each particle are shown, too.

CONCLUSIONS

In summary, the present work demonstrates strong and size-tunable Mie resonances in submicrometer Cu_2O cubes. The lowest energy Mie resonance observed in the extinction spectrum is assigned to the combination of the magnetic and electric dipole excitations. Similarly, both the magnetic and electric quadrupole excitations contribute to the second-lowest-energy Mie resonance peak observed in the extinction spectrum. The Mie resonance peak wavelengths are tunable from the visible to the near-IR region by controlling the size of the particles. By comparison, a higher scattering cross section is observed for Cu_2O cubes than spherical particles per equal size. Additionally, submicrometer Cu_2O cubes, being dielectric resonators, have scattering cross sections comparable to or slightly exceeding those of Ag particles. They exhibit enhancement of electric and magnetic fields for the incident light at Mie resonances. These high-performance nanoantenna attributes of the submicrometer Cu_2O cubic particles, combined with their low Ohmic losses and being semiconductors, make them attractive alternatives to PMNs in a wide range of applications, including spectroscopic, photonic, and energy-harvesting applications.

MATERIALS AND METHODS

The procedures for FDTD simulations, Cu_2O particles preparation, and UV−vis extinction and single-particle scattering measurements are described in detail in the Supporting Information. Briefly, we synthesized Cu_2O particles of varying sizes and shapes and confirmed the corresponding Mie resonance peaks using UV−vis extinction spectroscopy. Additionally, single-particle scattering measurements were used to confirm the strong scattering from Cu_2O cubes. To predict and compare the optical behavior of Cu_2O particles of varying sizes and shapes, we utilized the Lumerical FDTD package. The optical data for Cu_2O and Ag were obtained from Palik.[53]

ASSOCIATED CONTENT

Supporting Information

The Supporting Information is available free of charge at https://pubs.acs.org/doi/10.1021/acsanm.0c01201.

Detailed synthesis methods, experimental and characterization procedures, and FDTD simulation procedures (PDF)

AUTHOR INFORMATION

Corresponding Author

Marimuthu Andiappan − *School of Chemical Engineering, Oklahoma State University, Stillwater, Oklahoma 74078, United States;* orcid.org/0000-0002-4211-030X;
Email: mari.andiappan@okstate.edu

Authors

Farshid Mohammadparast − *School of Chemical Engineering, Oklahoma State University, Stillwater, Oklahoma 74078, United States*
Sundaram Bhardwaj Ramakrishnan − *School of Chemical Engineering, Oklahoma State University, Stillwater, Oklahoma 74078, United States*
Nishan Khatri − *School of Mechanical and Aerospace Engineering, Oklahoma State University, Stillwater, Oklahoma 74078, United States*
Ravi Teja A. Tirumala − *School of Chemical Engineering, Oklahoma State University, Stillwater, Oklahoma 74078, United States*
Susheng Tan − *Department of Electrical and Computer Engineering, University of Pittsburgh, Pittsburgh, Pennsylvania 15260, United States;* orcid.org/0000-0002-6162-7443
A. Kaan Kalkan − *School of Mechanical and Aerospace Engineering, Oklahoma State University, Stillwater, Oklahoma 74078, United States;* orcid.org/0000-0001-5878-3413

Complete contact information is available at:
https://pubs.acs.org/10.1021/acsanm.0c01201

Author Contributions

F.M. and S.B.R. contributed equally to this work..

Notes

The authors declare no competing financial interest.

ACKNOWLEDGMENTS

The research results discussed in this publication were made possible in part by funding through the award for project number HR18-093, from the Oklahoma Center for the Advancement of Science and Technology. Additionally, A.K.K. acknowledges funding by the National Science Foundation (Award #1707008). The TEM and SEM images were acquired at the Oklahoma State University (OSU) Microscopy Laboratory. We thank Dr. Andrej Lenert, University of Michigan, for helpful discussions.

REFERENCES

(1) Kelly, K. L.; Coronado, E.; Zhao, L. L.; Schatz, G. C. The Optical Properties of Metal Nanoparticles: The Influence of Size, Shape, and Dielectric Environment. *J. Phys. Chem. B* **2003**, *107* (3), 668−677.

(2) Ross, M. B.; Mirkin, C. A.; Schatz, G. C. Optical Properties of One-, Two-, and Three-Dimensional Arrays of Plasmonic Nanostructures. *J. Phys. Chem. C* **2016**, *120* (2), 816−830.

(3) Lu, X.; Rycenga, M.; Skrabalak, S. E.; Wiley, B.; Xia, Y. Chemical Synthesis of Novel Plasmonic Nanoparticles. *Annu. Rev. Phys. Chem.* **2009**, *60* (1), 167−192.

(4) Wiley, B.; Sun, Y.; Mayers, B.; Xia, Y. Shape-Controlled Synthesis of Metal Nanostructures: The Case of Silver. *Chem. - Eur. J.* **2005**, *11* (2), 454−463.

(5) Xia, Y.; Halas, N. J. Shape-Controlled Synthesis and Surface Plasmonic Properties of Metallic Nanostructures. *MRS Bull.* **2005**, *30* (5), 338−348.

(6) Sherry, L. J.; Chang, S.-H.; Schatz, G. C.; Van Duyne, R. P.; Wiley, B. J.; Xia, Y. Localized Surface Plasmon Resonance Spectroscopy of Single Silver Nanocubes. *Nano Lett.* **2005**, *5* (10), 2034−2038.

(7) Wang, H.; Brandl, D. W.; Nordlander, P.; Halas, N. J. Plasmonic Nanostructures: Artificial Molecules. *Acc. Chem. Res.* **2007**, *40* (1), 53−62.

(8) Marimuthu, A.; Christopher, P.; Linic, S. Design of Plasmonic Platforms for Selective Molecular Sensing Based on Surface-Enhanced Raman Spectroscopy. *J. Phys. Chem. C* **2012**, *116* (17), 9824−9829.

(9) Brus, L. Noble Metal Nanocrystals: Plasmon Electron Transfer Photochemistry and Single-Molecule Raman Spectroscopy. *Acc. Chem. Res.* **2008**, *41* (12), 1742−1749.

(10) Michaels, A. M.; Jiang; Brus, L. Ag Nanocrystal Junctions as the Site for Surface-Enhanced Raman Scattering of Single Rhodamine 6G Molecules. *J. Phys. Chem. B* **2000**, *104* (50), 11965−11971.

(11) Link, S.; El-Sayed, M. A. Optical Properties and Ultrafast Dynamics of Metallic Nanocrystals. *Annu. Rev. Phys. Chem.* **2003**, *54* (1), 331−366.

(12) Jarrett, J. W.; Zhao, T.; Johnson, J. S.; Knappenberger, K. L. Investigating Plasmonic Structure-Dependent Light Amplification and Electronic Dynamics Using Advances in Nonlinear Optical Microscopy. *J. Phys. Chem. C* **2015**, *119* (28), 15779−15800.

(13) Devaux, E.; Laluet, J.-Y.; Stein, B.; Genet, C.; Ebbesen, T.; Weeber, J.-C.; Dereux, A. Refractive Micro-Optical Elements for Surface Plasmons: From Classical to Gradient Index Optics. *Opt. Express* **2010**, *18* (20), 20610−20619.

(14) Linic, S.; Christopher, P.; Ingram, D. B. Plasmonic-Metal Nanostructures for Efficient Conversion of Solar to Chemical Energy. *Nat. Mater.* **2011**, *10* (12), 911−921.

(15) Christopher, P.; Xin, H.; Marimuthu, A.; Linic, S. Singular Characteristics and Unique Chemical Bond Activation Mechanisms of Photocatalytic Reactions on Plasmonic Nanostructures. *Nat. Mater.* **2012**, *11* (12), 1044−1050.

(16) Hou, W.; Cronin, S. B. A Review of Surface Plasmon Resonance-Enhanced Photocatalysis. *Adv. Funct. Mater.* **2013**, *23* (13), 1612−1619.

(17) Kamat, P. V. Photophysical, Photochemical and Photocatalytic Aspects of Metal Nanoparticles. *J. Phys. Chem. B* **2002**, *106* (32), 7729−7744.

(18) Li, J.; Cushing, S. K.; Meng, F.; Senty, T. R.; Bristow, A. D.; Wu, N. Plasmon-Induced Resonance Energy Transfer for Solar Energy Conversion. *Nat. Photonics* **2015**, *9* (9), 601−607.

(19) Cushing, S. K.; Li, J.; Meng, F.; Senty, T. R.; Suri, S.; Zhi, M.; Li, M.; Bristow, A. D.; Wu, N. Photocatalytic Activity Enhanced by Plasmonic Resonant Energy Transfer from Metal to Semiconductor. *J. Am. Chem. Soc.* **2012**, *134* (36), 15033−15041.

(20) Marimuthu, A.; Zhang, J.; Linic, S. Tuning Selectivity in Propylene Epoxidation by Plasmon Mediated Photo-Switching of Cu Oxidation State. *Science* **2013**, *339* (6127), 1590−1593.

(21) Thrithamarassery, G. D.; Xu, Z.; Liu, Y.; Izquierdo, R.; Ma, D. Recent Advancements in Plasmon-Enhanced Promising Third-Generation Solar Cells. *Nanophotonics* **2017**, *6* (1), 153−175.

(22) Sandén, S.; Akitsu, K.; Törngren, B.; Ylinen, A.; Smått, J.-H.; Kubo, T.; Matsumura, M.; Otani, N.; Segawa, H.; Österbacka, R. Plasmon-Enhanced Polymer-Sensitized Solar Cells. *J. Phys. Chem. C* **2015**, *119* (10), 5570−5576.

(23) Jang, Y. H.; Jang, Y. J.; Kim, S.; Quan, L. N.; Chung, K.; Kim, D. H. Plasmonic Solar Cells: From Rational Design to Mechanism Overview. *Chem. Rev.* **2016**, *116* (24), 14982−15034.

(24) Feng, L.; Niu, M.; Wen, Z.; Hao, X. Recent Advances of Plasmonic Organic Solar Cells: Photophysical Investigations. *Polymers* **2018**, *10* (2), 123.

(25) Şarlı, N. Artificial Magnetism in a Carbon Diamond Nanolattice with the Spin Orientation Effect. *Diamond Relat. Mater.* **2016**, *64*, 103.

(26) Cong, J.; Zhou, Z.; Yun, B.; Yao, H.; Ren, N. Artificial Magnetism of Cross Shaped Metamaterial in Green Light Frequencies. *Opt. Mater.* **2015**, *50*, 123−127.

(27) Markovich, D.; Baryshnikova, K.; Shalin, A.; Samusev, A.; Krasnok, A.; Belov, P.; Ginzburg, P. Enhancement of Artificial Magnetism via Resonant Bianisotropy. *Sci. Rep.* **2016**, *6*, 22546.

(28) Liu, Y.; Zhang, X. Metasurfaces for Manipulating Surface Plasmons. *Appl. Phys. Lett.* **2013**, *103* (14), 141101.

(29) Cai, W.; Chettiar, U. K.; Kildishev, A. V.; Shalaev, V. M. Optical Cloaking with Metamaterials. *Nat. Photonics* **2007**, *1* (4), 224−227.

(30) Shin, D.; Urzhumov, Y.; Jung, Y.; Kang, G.; Baek, S.; Choi, M.; Park, H.; Kim, K.; Smith, D. R. Broadband Electromagnetic Cloaking with Smart Metamaterials. *Nat. Commun.* **2012**, *3* (1), 1−8.

(31) Cortés, L. R.; Seghilani, M.; Maram, R.; Azaña, J. Full-Field Broadband Invisibility through Reversible Wave Frequency-Spectrum Control. *Optica* **2018**, *5* (7), 779−786.

(32) Duan, X.; Kamin, S.; Liu, N. Dynamic Plasmonic Colour Display. *Nat. Commun.* **2017**, *8*, 14606.

(33) Kuznetsov, A. I.; Miroshnichenko, A. E.; Brongersma, M. L.; Kivshar, Y. S.; Luk'yanchuk, B. Optically Resonant Dielectric Nanostructures. *Science* **2016**, *354* (6314), No. aag2472.

(34) Manthiram, K.; Alivisatos, A. P. Tunable Localized Surface Plasmon Resonances in Tungsten Oxide Nanocrystals. *J. Am. Chem. Soc.* **2012**, *134* (9), 3995−3998.

(35) Mattox, T. M.; Ye, X.; Manthiram, K.; Schuck, P. J.; Alivisatos, A. P.; Urban, J. J. Chemical Control of Plasmons in Metal Chalcogenide and Metal Oxide Nanostructures. *Adv. Mater.* **2015**, *27* (38), 5830−5837.

(36) Krasnok, A.; Makarov, S.; Petrov, M.; Savelev, R.; Belov, P.; Kivshar, Y. Towards All-Dielectric Metamaterials and Nanophotonics. arXiv:1503.08857 [physics], **2015**.

(37) Kruk, S.; Kivshar, Y. Functional Meta-Optics and Nanophotonics Govern by Mie Resonances. arXiv:1710.08595 [physics], **2017**.

(38) García-Etxarri, A.; Gómez-Medina, R.; Froufe-Pérez, L. S.; López, C.; Chantada, L.; Scheffold, F.; Aizpurua, J.; Nieto-Vesperinas, M.; Sáenz, J. J. Strong Magnetic Response of Submicron Silicon Particles in the Infrared. *Opt. Express* **2011**, *19* (6), 4815.

(39) Zhang, J.; MacDonald, K. F.; Zheludev, N. I. Near-Infrared Trapped Mode Magnetic Resonance in an All-Dielectric Metamaterial. *Opt. Express* **2013**, *21* (22), 26721.

(40) Evlyukhin, A. B.; Reinhardt, C.; Chichkov, B. N. Multipole Light Scattering by Nonspherical Nanoparticles in the Discrete Dipole Approximation. *Phys. Rev. B: Condens. Matter Mater. Phys.* **2011**, DOI: 10.1103/PhysRevB.84.235429.

(41) Grzela, G.; Paniagua-Domínguez, R.; Barten, T.; Fontana, Y.; Sánchez-Gil, J. A.; Gómez Rivas, J. Nanowire Antenna Emission. *Nano Lett.* **2012**, *12* (11), 5481−5486.

(42) Cao, L.; Fan, P.; Vasudev, A. P.; White, J. S.; Yu, Z.; Cai, W.; Schuller, J. A.; Fan, S.; Brongersma, M. L. Semiconductor Nanowire Optical Antenna Solar Absorbers. *Nano Lett.* **2010**, *10* (2), 439−445.

(43) Cao, L.; White, J. S.; Park, J.-S.; Schuller, J. A.; Clemens, B. M.; Brongersma, M. L. Engineering Light Absorption in Semiconductor Nanowire Devices. *Nat. Mater.* **2009**, *8* (8), 643−647.

(44) Schuller, J. A.; Zia, R.; Taubner, T.; Brongersma, M. L. Dielectric Metamaterials Based on Electric and Magnetic Resonances of Silicon Carbide Particles. *Phys. Rev. Lett.* **2007**, *99* (10), 107401.

(45) Person, S.; Jain, M.; Lapin, Z.; Sáenz, J. J.; Wicks, G.; Novotny, L. Demonstration of Zero Optical Backscattering from Single Nanoparticles. *Nano Lett.* **2013**, *13* (4), 1806−1809.

(46) Ginn, J. C.; Brener, I.; Peters, D. W.; Wendt, J. R.; Stevens, J. O.; Hines, P. F.; Basilio, L. I.; Warne, L. K.; Ihlefeld, J. F.; Clem, P. G.; Sinclair, M. B. Realizing Optical Magnetism from Dielectric Metamaterials. *Phys. Rev. Lett.* **2012**, *108* (9), 097402.

(47) Rybin, M. V.; Filonov, D. S.; Samusev, K. B.; Belov, P. A.; Kivshar, Y. S.; Limonov, M. F. Phase Diagram for the Transition from Photonic Crystals to Dielectric Metamaterials. *Nat. Commun.* **2015**, *6* (1), 1−6.

(48) Ruan, Q.; Li, N.; Yin, H.; Cui, X.; Wang, J.; Lin, H.-Q. Coupling between the Mie Resonances of Cu_2O Nanospheres and the Excitons of Dye Aggregates. *ACS Photonics* **2018**, *5* (9), 3838−3848.

(49) Susman, M. D.; Vaskevich, A.; Rubinstein, I. Refractive Index Sensing Using Visible Electromagnetic Resonances of Supported Cu_2O Particles. *ACS Appl. Mater. Interfaces* **2017**, *9* (9), 8177−8186.

(50) Zhang, L.; Wang, H. Cuprous Oxide Nanoshells with Geometrically Tunable Optical Properties. *ACS Nano* **2011**, *5* (4), 3257−3267.

(51) Tirumala, R. T. A.; Dadgar, A. P.; Mohammadparast, F.; Ramakrishnan, S. B.; Mou, T.; Wang, B.; Andiappan, M. Homogeneous versus Heterogeneous Catalysis in Cu_2O-Nanoparticle-Catalyzed C−C Coupling Reactions. *Green Chem.* **2019**, *21*, 5284−5290.

(52) Mao, Y.; He, J.; Sun, X.; Li, W.; Lu, X.; Gan, J.; Liu, Z.; Gong, L.; Chen, J.; Liu, P.; Tong, Y. Electrochemical Synthesis of Hierarchical Cu_2O Stars with Enhanced Photoelectrochemical Properties. *Electrochim. Acta* **2012**, *62*, 1−7.

(53) Powell, D.; Compaan, A.; Macdonald, J. R.; Forman, R. A. Raman-Scattering Study of Ion-Implantation-Produced Damage in Cu_2O. *Phys. Rev. B* **1975**, *12* (1), 20−25.

(54) Niveditha, C. V.; Fatima, M. J. J.; Sindhu, S. Comprehensive Interfacial Study of Potentio-Dynamically Synthesized Copper Oxide Thin Films for Photoelectrochemical Applications. *J. Electrochem. Soc.* **2016**, *163* (6), H426−H433.

(55) Sander, T.; Reindl, C. T.; Giar, M.; Eifert, B.; Heinemann, M.; Heiliger, C.; Klar, P. J. Correlation of Intrinsic Point Defects and the

Raman Modes of Cuprous Oxide. *Phys. Rev. B: Condens. Matter Mater. Phys.* **2014**, *90* (4), 1−8.

(56) Wang, Z.; Pischedda, V.; Saxena, S. K.; Lazor, P. X-Ray Diffraction and Raman Spectroscopic Study of Nanocrystalline CuO under Pressures. *Solid State Commun.* **2002**, *121* (5), 275−279.

(57) Wu, H.-W.; Chen, H.-J.; Xu, H.-F.; Fan, R.-H.; Li, Y. Tunable Multiband Directional Electromagnetic Scattering from Spoof Mie Resonant Structure. *Sci. Rep.* **2018**, *8* (1), 8817.